Università degli Studi di Genova

Scuola Politecnica
DIME

Dipartimento di Ingegneria Meccanica, Energetica
Gestionale e dei Trasporti

Tesi di laurea triennale in

Ingegneria Meccanica

Fluid flow over slippery surfaces

Allievo
Remo Fadda

Supervisore
Ch.mo Prof. Alessandro Bottaro

Co-Supervisore
Dr. Essam Nabil Ahmed

Luglio 2024

A Niccolò e Letizia.

Prefazione

Questa tesi si propone di studiare il comportamento di un moto fluido su una parete scabra infusa di lubrificante, quantificando la peculiare caratteristica di slittamento che questa classe di superfici presenta e la possibile riduzione di resistenza d'attrito. L'analisi è stata condotta sia per superfici superidrofobiche che per quelle infuse da un lubrificante liquido, comunemente chiamate "LIS". Lo studio è principalmente relativo al moto fluido in regime laminare, ma vengono anche presentati alcuni risultati per il caso turbolento.

La prima parte della tesi presenta un approccio teorico alla formulazione del problema, fornendo inoltre una breve panoramica sulla teoria dell'omogeneizzazione asintotica e delle condizioni al contorno *effetive* adottate.
La seconda parte, invece, riporta i risultati ottenuti tramite simulazioni numeriche, i quali mostrano l'influenza che caratteristiche geometriche e perdita di lubrificante hanno sul termine di slittamento λ.

Abstract

This work aims to investigate the behaviour of a fluid flow over a rough surface infused by a lubricant, by quantifying the slip that these surfaces can produce and the possible reduction in the skin-friction drag. The analysis has been conducted for both superhydrophobic and liquid-infused configurations. The study is mainly concerned with the laminar flow regime, although some results for turbulence are reported and discussed.

In the first part of the thesis, a theoretical formulation for the problem is described, providing insights on the application of the asymptotic homogenization theory and the upscaled *effective* boundary conditions adopted. Later, the Navier-slip length λ is evaluated numerically for surfaces with different geometric features, highlighting the role of lubricant depletion. The consequent effects on the skin-friction drag and on the flow rate through the channel are assessed.

Contents

Symbology **1**

1 Introduction **3**

2 State of the Art **4**
- 2.1 A new frontier in drag reduction . . . 4
- 2.2 Drag reduction framework . . . 5
- 2.3 One case of experimental research . . . 7
- 2.4 The depletion problem . . . 9
- 2.5 Nanobubbles: a potential explanation to the slip observed on LIS . . . 11

3 Theoretical Formulation **13**
- 3.1 Initial equations . . . 14
- 3.2 Evaluation of the Navier-slip coefficient . . . 15
- 3.3 An additional scenario . . . 16

4 Asymptotic Homogenization **17**
- 4.1 Governing equations and boundary conditions . . . 17
- 4.2 Asymptotic analysis . . . 20
- 4.3 Effective boundary conditions . . . 21

5 Modelling and Simulation of Superhydrophobic and Liquid-Infused Surfaces **23**
- 5.1 CFD software . . . 23
- 5.2 Superhydrophobic surfaces . . . 26
- 5.3 MATLAB code . . . 30
- 5.4 Liquid-infused surfaces . . . 31
  - 5.4.1 Numerical approach . . . 31
  - 5.4.2 A look into the literature . . . 32

6 What about Turbulence? **34**

7 Conclusions **36**

Symbology

Symbols

H	Half-channel height
e	Square groove's size
p	Pressure
$\mathbf{u}$	Velocity vector
μ	Dynamic viscosity
λ	Navier-slip coefficient
Q	Volumetric flow rate
ϵ	Ratio of the length scales
l	Microscopic length scale
L	Macroscopic length scale
ρ	Density
t	Time
Re	Macroscopic Reynolds number
$\mathcal{R}$	Microscopic Reynolds number
$\mathcal{I}_{\beta\sigma}$	Fluid-solid interface
$\mathbf{S}$	Traction vector
k^{itf}	Interface permeability coefficient
α	Lubricant area fraction
d	Depletion

ϕ_s	Solid area fraction
μ_R	Viscosity ratio
u_τ	Shear velocity
τ_w	Shear stress
ΔU^+	Roughness function
c_f	Friction factor
k	Von Karman constant
Re_τ	Shear velocity Reynolds number

1 Introduction

Efficient drag-reducing techniques are capable of reducing wall friction for a given flow rate over the surface or increasing the fluid flow under a given driving pressure gradient. Thanks to its economic and environmental benefits, achieving drag reduction is a crucial step in the design of any system interacting with a fluid flow in relative motion. Much of the research on drag reduction in both laminar and turbulent flows is focused on modifying the no-slip wall boundary condition. Regarding this, superhydrophobic surfaces (SHS) are an excellent solution to the problem, due to their capability of reducing drag in water flows by up to 50%.

SHS are gas-cushioned surfaces where air fills the roughness of the wall. This feature can be achieved using chemical treatments so that the surface is functionalized to have large contact angles for water, which is essential in maintaining the air inside the asperities when the wall is submerged. Due to the much smaller viscosity of air than that of water, the shear in the regions where the fluid slips over the air-filled cavities is widely reduced; the shear in the rest of the wall remains large as a consequence of the no-slip condition. If the local shear stress is integrated over the entire surface, a remarkable decrease in drag can be noticed.

However, SHS have some significant drawbacks. The main issue is related to the air-water interface, which originates once the working fluid flows over the air pockets. Experiments indicate that this interface is prone to collapse under pressure fluctuations and physical stresses, which would allow the gas to dissolve into the liquid. Once the asperities are partially or totally flooded with water, the drag-reducing mechanism deteriorates and even a drag increase relative to the case of a smooth no-slip surface can take place. Therefore, SHS are not ideal for several practical applications.

In this regard, a new class of surfaces have been recently studied as a potential alternative, where a liquid lubricant infuses the solid surface, filling the roughness of the wall as well. The presence of a liquid lubricant enhances the performance of the surface in terms of interface stability between the external flow and the lubricant, maintaining at the same time the ability to reduce drag.

The aim of this work is to investigate and quantify the effective slip over both superhydrophobic and liquid-infused surfaces, and to understand their potentiality in real world's applications.

2 State of the Art

2.1 A new frontier in drag reduction

Liquid-infused surfaces (LIS) are a novel, passive method of drag reduction.
They are inspired by the the Nepenthes Pitcher Plants, which rely on the movement of liquid lubricants to facilitate mobility of the fluid-fluid interface [1].
The interest in this new class of surfaces results from the need to enhance the performance of superhydrophobic surfaces.
LIS are composed of a liquid lubricant that is trapped within chemically matched roughness elements and is immiscible with external fluids. The presence of a lubricant offers several benefits. The liquid-lubricant interface is slippery, preventing the attachment of microorganisms and resulting in an anti-fouling surface [2][3], which is instrumental, for example, in naval applications. Additionally, the slipping effect that occurs when the external fluid flows over the lubricant reduces the frictional resistance exerted on the surface [4][5]. Finally, the shear at the fluid-fluid interface exerted by the external flow over the trapped lubricant can set it in a recirculating motion, as shown in figure 2.1b, enhancing heat and mass transfer rate between the solid surface and the external fluid [6].

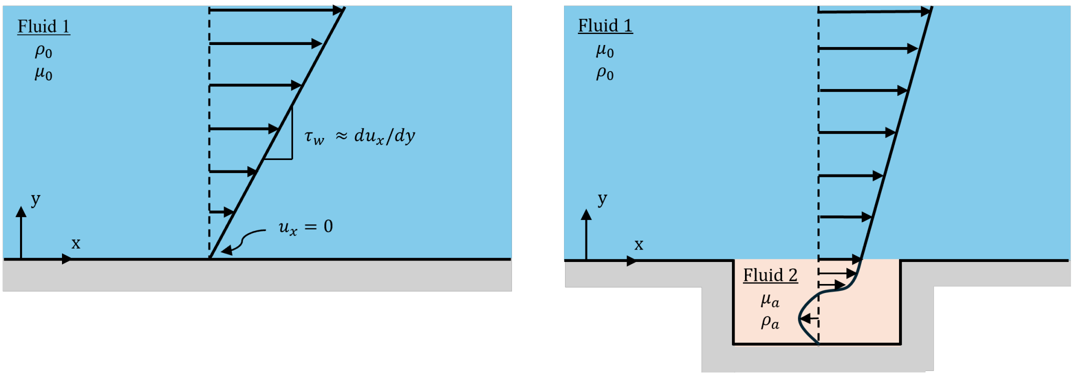

Figure 2.1: Flow over a solid surface: the no-slip condition holds everywhere (left). Flow over a groove filled with lubricant: the velocity at the liquid-lubricant interface is non-zero (right).

At present, liquid-infused surfaces represent the most significant alternative to SHS due to their inherently robustness to pressure changes, which provides integrity at the fluid-fluid interface, preventing a rapid depletion of the lubricant from the pockets. As mentioned by Van Buren & Smits (2017) in their study [7], there are two significant parameters that guarantee the integrity of the interface: Bond and Weber numbers.
The Bond number $Bo = (\rho_e - \rho_l)gl^2/\gamma$, is defined as the ratio of the buoyancy force to the capillary force. ρ_e and ρ_l are, respectively, the densities of the external and lubricant fluids, l is the characteristic length scale of the surface asperities and γ is the interfacial tension. Since the lubricant and the external fluid have different densities, the resulting buoyancy force can deplete the lubricant by overcoming the capillary force holding the fluid in. The Weber number $We = \rho_e u^2 l/\gamma$, is the ratio between

the inertial force and the capillary force. A large value of the Weber number means that the inertia force can overcome the capillary force and allow the infused liquid to escape. The infused and the external liquids need to be immiscible for a good performance, since even a small depletion of lubricant will cause an overall drag increase [8], so both the Weber and Bond numbers need to be small to avoid failure. Other fundamental parameters governing the performance of LIS are: the viscosity ratio $N = \mu_e/\mu_l$, where μ_e and μ_l are the viscosities of the external and lubricating fluids. The Reynolds number $Re = \rho_e ul/\mu_e$, where u is the characteristic flow velocity and l is a characteristic length scale; Reynolds number is the ratio of the inertial forces to the viscous forces. And last, the surface geometry. A common parameter used to express the geometry feature of the problem is the fluid area fraction $a = A_l/A_t$, where A_l is the surface area of the exposed lubricant fluid and A_t is the total surface area.

2.2 Drag reduction framework

To fully understand how LIS work, we need to give a closer look at the coupling between the lubricant and the working fluid.

Since a liquid lubricant will most likely have a considerably higher viscosity compared to air, infusing the lubricant for the benefit of fluid-fluid interfacial stability can be detrimental from the viewpoint of drag reduction.

As previously mentioned, on LIS, regions of small intrinsic slip (originating from low molecular interactions between the solid wall and the working fluid) are interspersed with regions of large slip (in which the working fluid is in contact with the lubricant). When the external fluid flows over the latter scenario, recirculation occurs inside the pockets filled with lubricant, which supports a finite interfacial slip velocity.

Let's consider an example where a working fluid flows over a groove filled with lubricant. The two fluids are chosen to be immiscible and to maintain a flat interface. Two conditions are applied:

$$\begin{cases} u_e = u_l \\ \dfrac{1}{\mu_e}\dfrac{\partial u_e}{\partial y}\bigg|_i = \dfrac{1}{\mu_l}\dfrac{\partial u_l}{\partial y}\bigg|_i \end{cases} \tag{2.1}$$

where u_e and u_l are the velocities of the external and lubricating fluids respectively, and $\partial u/\partial y$ is the surface-normal gradient of the streamwise velocity.

These conditions state that, locally along the interface, the external fluid and the lubricant must both exhibit the same velocity and shear stress.

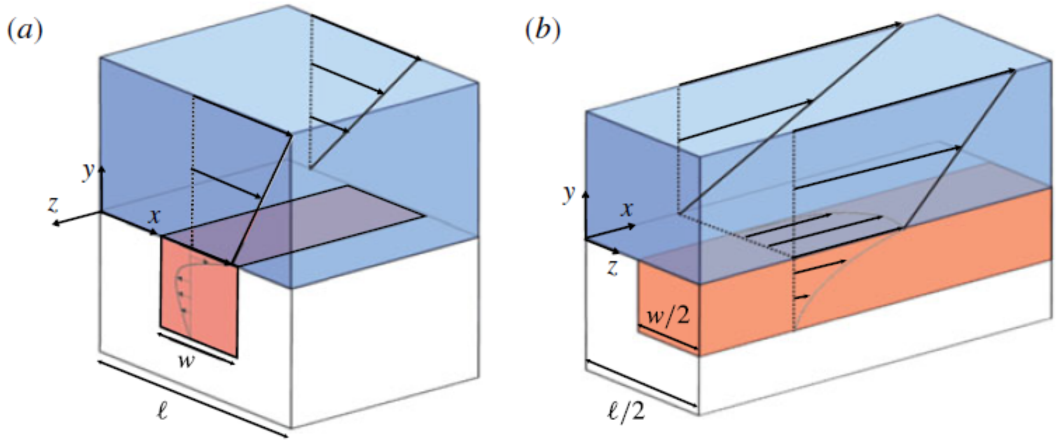

Figure 2.2: Fluid flow over LIS in spanwise configuration (a) and streamwise configuration (b). Illustration from Fu et al. (2017) [1]

The slip velocity established at the interface is the essential responsible for drag reduction, because the external flow will have a smaller local velocity gradient over the liquid-lubricant interface compared to the flow over the no-slip regions.

In particular, the second matching condition shows that if the two fluid have different dynamic viscosities, there will be a discontinuity in the velocity gradient at the interface. As the viscosity within the roughness increases, the fluid-fluid interface is able to sustain a higher slip velocity.

The interfacial slip is quantified with the slip length, which is the imaginary distance beyond the solid wall at which the linear extrapolation of the fluid velocity vanishes to zero.

Since large local slip does not always translate into an overall slip effect, due for example to the presence of impurities of the asperities, it is common to characterize LIS with an effective slip length λ: the equivalent slip required on a smooth surface that would produce the same flow conditions far away from the composite surface. Effective drag reduction involves the integration of all the individual, localized slipping effects along the fluid-lubricant interfaces as a macroscopic boundary condition for the flow.

2.3 One case of experimental research

Experiments have been conducted to understand the potential of LIS in practical applications. In particular, the work from Van Buren & Smits [7] reached a drag reduction using LIS as high as 35%.
The experiment were conducted in a Taylor-Couette rheometer facility, where an outer cylinder rotates around the inner treated one. The latter presents longitudinal grooves on the lateral surface.
The gap between the two cylinders is $d = R_o - R_i = 2mm$, where R_o and R_i are respectively the radius of the outer and the inner cylinders, and the cylinder height is $H = 80mm$.
Once the outer cylinder is put into rotation at angular velocity ω, it causes characteristic surface velocity $u = \omega R_o$ and a torque T on the stationary inner cylinder.
The characteristic dimension of the grooves is w, ranging from 100 μm to 800 μm, to better understand the impact of the size of the features.

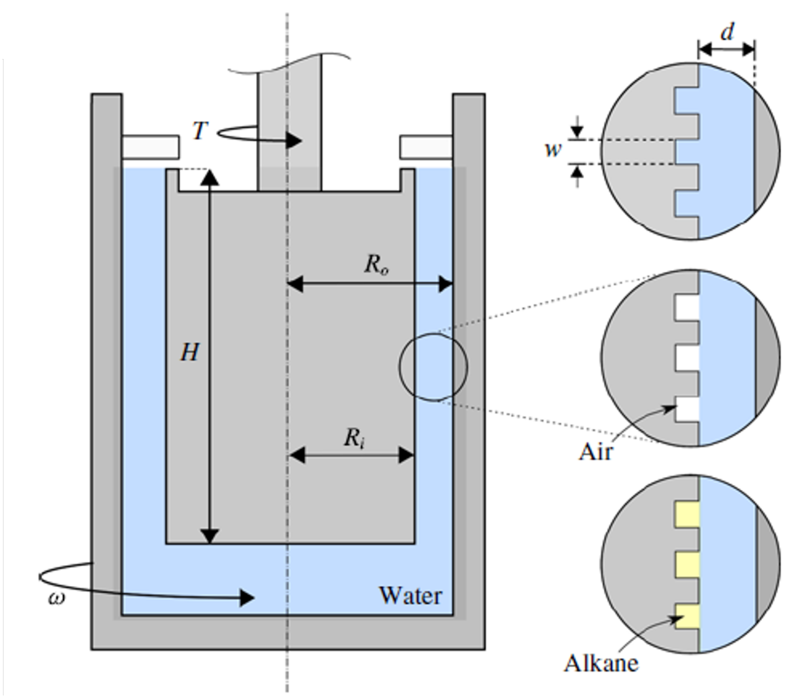

Figure 2.3: Experimental set-up of the Taylor-Couette facility. Illustration from Van Buren & Smits [7].

Longitudinal grooves were tested with water, as a baseline case, air and alkane oils. To obtain a liquid-infused surface, the inner cylinder were firs dip-coated in the infused liquid, and then immediately submerged in water in order to limit the exposure of the lubricant to air, since the lower-viscosity alkanes are very volatile. The tests were conducted measuring the torque performed on the inner cylinder, which is related to the drag reduction as follows: $DR = (T_0 - T)/T_0$, where T_0 is the torque measured in the baseline case with water inside the grooves.
Results show that generally the torque increases with Reynolds number because at higher spin rates there's more friction drag on the inner cylinder. But they also show

that employing air or alkanes liquids decreases the cylinder torque at fixed Reynolds number. In addition, for all groove sizes the measures exhibit a general trend where higher viscosity ratios result in a larger drag reduction.

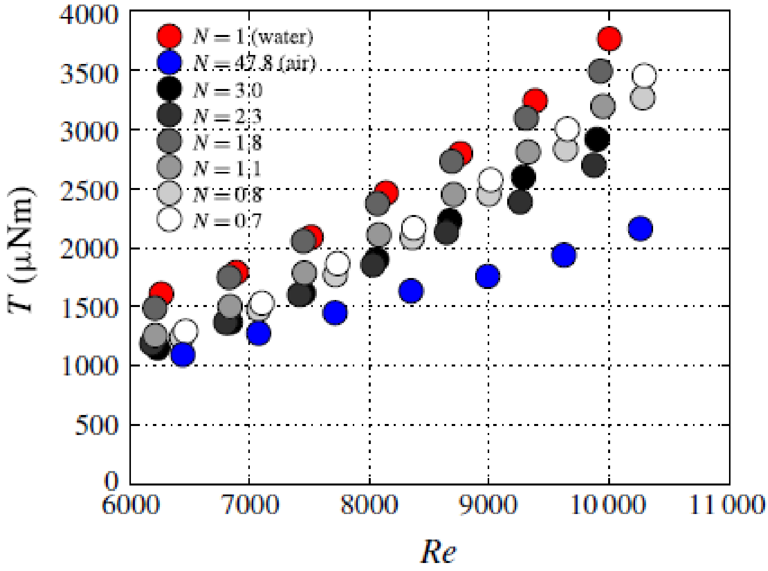

Figure 2.4: Cylinder torque as a function of Reynolds number for several cases represented by their viscosity ratio. In this case, w is fixed at $400\mu m$. Illustration from Van Buren & Smits (2017) [7].

As shown in figure 2.4, there are some higher-viscosity oils that produce larger drag reduction than the lower-viscosity cases, particularly for the $w = 400\mu m$ case. This in unexpected, and the most likely cause of this behaviour is surface failure of the lower-viscosity oils, possibly due to instabilities on the interface.

For the largest groove size, $w = 800\mu m$, at the higher Reynolds numbers, the drag reduction decreases with increasing Reynolds number. But this was explained by a visual inspection, showing a partial failure under these conditions. Increasing the fluid area fraction also helped in increasing the level of drag reduction.

In conclusion, the experimental tests demonstrated that a drag reduction in turbulent Taylor-Couette flow with liquid-infused surfaces was not only possible, but reached excellent results comparable to the performance of SHS.

2.4 The depletion problem

Despite their excellent characteristics, liquid-infused surfaces suffer from a significant problem. It seems that even a slight lubricant loss decreases slip to the point of making the lubricant superfluous.
Most of the models used to study LIS assume that the fluid-lubricant interface is pinned at the top of the surface topography and is flat and non-deformable. However, under realistic conditions, the interface is not pinned at the top of the surface topography and lubricant depletion occurs due to the shear stress or static pressure imposed by the external fluid.
A study from Vega-Sánchez & Neto (2022) [8] investigated the behaviour of partially filled cavities, and also the effect on slip of the position and the curvature of the fluid-lubricant interface.
They reported numerical simulations that quantify the effective fluid slip over a LIS containing grooves filled with lubricant, oriented perpendicular to the flow direction.

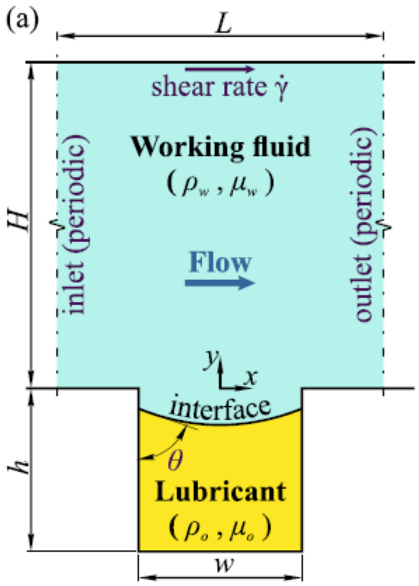

Figure 2.5: Definition of the parameters used to model a Couette flow over transverse grooves in the case of partially filled groove. Illustration from Vega-Sánchez & Neto (2022) [8].

To investigate the effective slip in a domain where the interface is not pinned at the top of the groove, two parameters are defined: one is the lubricant filled ratio $\psi = V_o - V_c$, where V_o and V_c correspond to the lubricant and cavity volume, respectively. And the other is the lubricant contact angle θ, which is defined as the angle formed between the fluid-lubricant interface and the fluid-solid interface.
The results from their work show that the effective slip length strongly depends on the lubricant contact angle and reaches a maximum value for a slightly protruding interface ($\theta = 107°$), and increases with increasing the viscosity ratio.
In addition, they demonstrated that for a wetting lubricant ($\theta \sim 30°$) which produces a highly concave interface, the slip length is no larger than in the case with no lubricant at all, regardless of the viscosity of the lubricant. This is also in direct

conflict with the previous studies on LIS, where a common practice to increase lubricant retention was to select lubricants which fully wet the solid substrate.

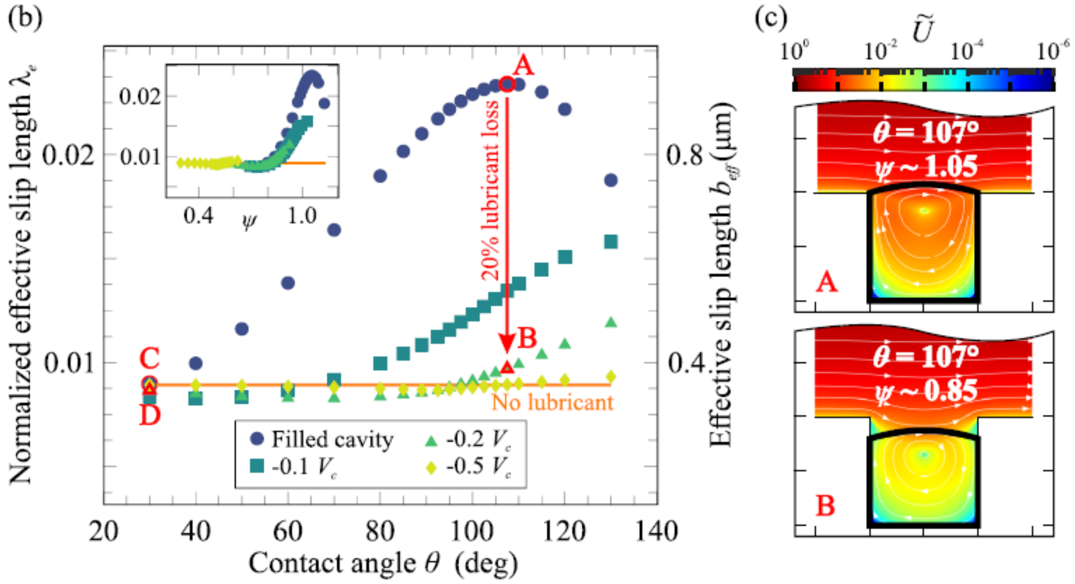

Figure 2.6: (b) Effect of lubricant loss on effective slip length λ_e as a function of the contact angle θ. Here, the viscosity ratio N = 10 is representative of a realistic liquid lubricant scenario. (c) Normalized velocity magnitude for the cases A and B in panel b. The streamlines are shown in white, and the lubricant volume is highlighted with a thick black line. Illustration from Vega-Sánchez & Neto (2022) [8].

As shown in figure 2.6b, a lubricant loss of just 10% of the cavity volume induces a drastic decrease of the slip length; when the lubricant loss is 20 and 50% of V_c, the values of the effective slip length λ_e are equal to the case of no lubricant in the cavity. Also, once the lubricant loss is larger than 20% of the cavity volume, the decrease in λ_e is the same regardless of the contact angle θ and therefore the shape of the interface. This demonstrate how λ_e is much more sensitive to changes in the filling ratio ψ than of the contact angle, meaning that lubricant depletion affects the slip length more than the shape of the interface itself.

With regard to the fully filled cavity case, they found that a slightly concave or convex interface offers a ball bearing effect to the working fluid, enhancing the overall slip in the system. However, strongly concave interfaces lose this effect as the external fluid is forced to enter in the cavity. On the other hand, highly convex interfaces are an obstacle for the flow, which negatively impacts the effective slip length.

In the partially filled case, the ball bearing effect is decreased by the fact that the interface is below the corners of the cavity, causing the external fluid to enter into the cavity.

2.5 Nanobubbles: a potential explanation to the slip observed on LIS

So far, liquid-infused surfaces seem to be an excellent substitute to SHS, providing a significant drag reduction.

Several studies have found that LIS are able to reduce frictional drag even when the viscosity of the lubricant is larger than that of the working fluid, which is quite counterintuitive. Indeed, very few explanations for this discrepancy have been provided, such as low sensitivity of experimental measurements or large variation in the surface roughness resulting in large uncertainty in the quantification of the slip length.

Recently, a study from Neto *et al.* (2022) [9], have found a disruptive discovery that could explain the large interfacial slip observed on LIS. They investigated the flow of water across microchannels over nanowrinkled Teflon surfaces, in both superhydrophobic and liquid-infused states.

The measurements revealed the nucleation of nanobubbles of the thickness of the order of 100 *nm* in plain Milli-Q water. In addition, the magnitude of the slip length was seen to increase with increasing the air content in the flowing water.

The main reasons why nanobubbles nucleation in LIS has never been taken into account are: the assumption that when the lubricant is depleted, the external fluid immediately fills the gaps, and the fact that acquiring experimental evidences of nanobubbles on a structured surface is very complex. The researchers of this study were able to identify this unexpected phenomenon thanks to their ability to map at the same time the lubricant film and the nanobubbles underwater.

To image directly nanobubbles on LIS they used meniscus force measurements: a subset of atomic force microscopy (AFM) force spectroscopy in which the dominant force on the cantilever is due to the formation of a liquid meniscus around the AFM tip [10].

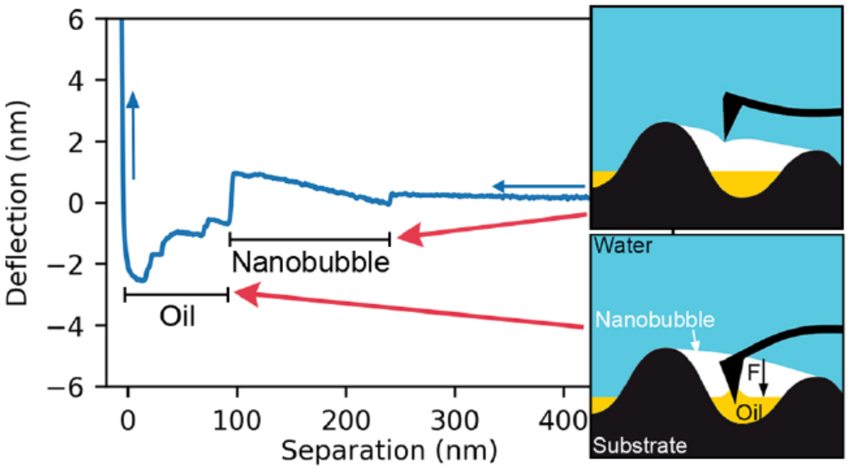

Figure 2.7: Force curve from which the nanobubbles and oil thicknesses are extracted (left). AFM tip approaching a nanobuble over a layer of oil (right). Illustration from Neto et al. (2022) [10].

A significant reduction in the pressure drop was measured when water flowed over infused surfaces [9]. The large slip observed in their experiments have been explained as a consequence of two factors: the recirculation within the lubricant pockets, which occurs since the velocity and shear stress in the flowing fluid are expected to match those in the lubricant interface, forcing the lubricant into a recirculating motion; the effect due to the presence of a lubricant of much lower viscosity, such as air, that would produce an easily observable reduction in the pressure drop. The nucleation of bubbles is due to the air dissolved in the water and in the lubricant, and they stick on exposed areas of the surface roughness. Once formed, the bubbles are stable under the imposed conditions. In addition, this stability was confirmed by the fact that the drag reduction effect was maintained for more than 24 hours. Since the lubricant is free to flow over the bubbles, it is possible that a oil layer can reduce the rate of air dissolution from the bubble into the external fluid.

As mentioned in the study, the effect of the nanobubbles on the slip is twofold: they reduce the overall roughness of the surface and provide a shear-free interface which significantly increases the local slip in comparison with the liquid lubricant counterpart.

The presence of air bubbles would explain the counterintuitive phenomena where a huge slip is observed even when the viscosity of the lubricant is larger than that of the working fluid. However, other studies need to be done to confirm the presence of nanobubbles and to well understand their mechanism of creation and effect on slip.

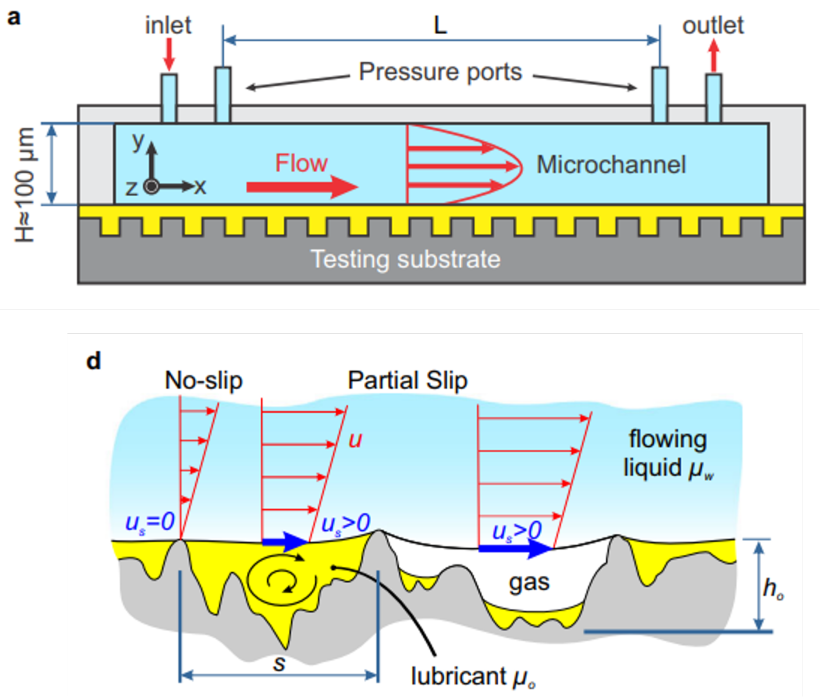

Figure 2.8: (a) Schematic set-up of the microchannel used in their study. The external fluid is water (blue), flowing from inlet to outlet over the lubricant (yellow) infused surface.
(b) Flow over a lubricant-infused rippled surface containing a nanobubble. Illustration from Neto et al. (2022) [9].

3 Theoretical Formulation

The problem is approached by analyzing two different scenarios: the first one is a bi-dimensional, laminar, fully developed Poiseuille flow in a channel, which is the baseline case. The height of the channel is $2H$. In the second one, the same flow conditions are applied, but the structure of the solid wall is different. The surface of the channel presents patterned square grooves filled with lubricant. We call e the characteristic dimension of the grooves.

In the latter case, a finite velocity is supported at the interface between the working flow and the lubricant inside the grooves, reducing the overall area of zero-slip at the wall compared with the baseline case. Also, the presence of these protrusions within the channel reduces the cross section area, and therefore decreases the bulk flow.

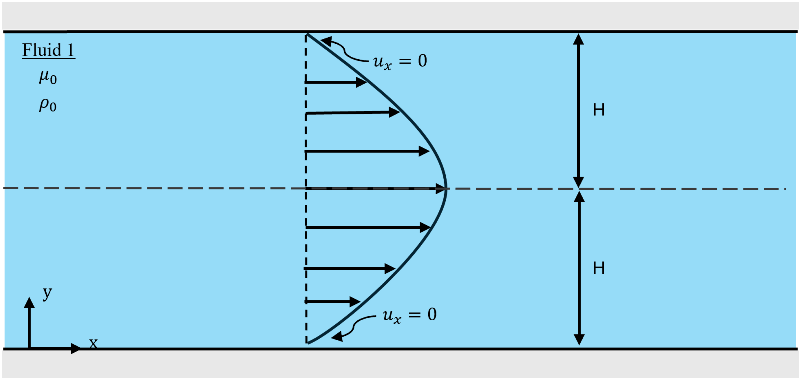

Figure 3.1: Laminar, fully developed Poiseuille flow in a smooth channel: the no-slip condition holds everywhere.

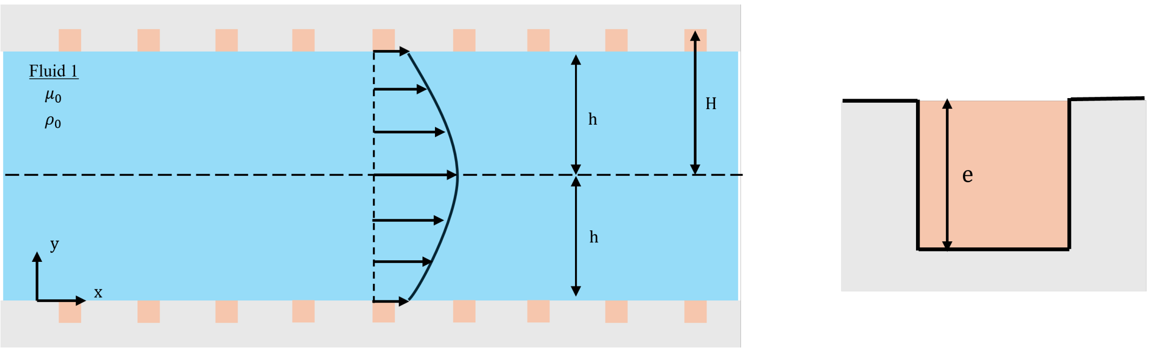

Figure 3.2: Flow in a channel where boundary walls present square grooves filled with lubricant. The velocity at the walls takes a finite values at the fluid-lubricant interface.

3.1 Initial equations

We start from the laminar, steady, incompressible Navier-Stokes momentum equation for a newtonian fluid

$$0 = -\frac{\partial \hat{p}}{\partial \hat{x}} + \mu \frac{\partial^2 \hat{u}}{\partial \hat{y}^2} \tag{3.1}$$

Note that every parameter that presents the "$\hat{.}$" symbol is dimensional in space and/or time.
The integration of the momentum equation results in the following velocity profile:

$$\mu \hat{u} = \frac{\partial \hat{p}}{\partial \hat{x}} \frac{\hat{y}^2}{2} + c_1 \hat{y} + c_2 \tag{3.2}$$

Two boundary conditions are applied to found c_1 and c_2. The fist one is the Navier-slip condition, which imposes that at the fluid-lubricant interface the normal velocity gradient is proportional to the slip length $\hat{\lambda}_x$. Whereas the second condition exploit the symmetry of the problem.

$$\begin{cases} \hat{y} = e \rightarrow \hat{u} = \hat{\lambda}_x \dfrac{\partial \hat{u}}{\partial \hat{y}} \\ \hat{y} = H \rightarrow \dfrac{\partial \hat{u}}{\partial \hat{y}} = 0 \end{cases} \tag{3.3}$$

By applying the boundary conditions the values for c_1 and c_2 are determined:

$$c_1 = -H \frac{\partial \hat{p}}{\partial \hat{x}} \qquad\qquad c_2 = \mu \hat{\lambda}_x \frac{\partial \hat{u}}{\partial \hat{y}}\bigg|_{y=e} - \frac{\partial \hat{p}}{\partial \hat{x}} \frac{e^2}{2} + H \frac{\partial \hat{p}}{\partial \hat{x}} e \tag{3.4}$$

where

$$\mu \frac{\partial \hat{u}}{\partial \hat{y}}\bigg|_{y=e} = \frac{\partial \hat{p}}{\partial \hat{x}} e - \frac{\partial \hat{p}}{\partial \hat{x}} H \tag{3.5}$$

The velocity profile of the working fluid flow is therefore:

$$\hat{u} = \frac{1}{\mu} \frac{\partial \hat{p}}{\partial \hat{x}} \left(\frac{y^2}{2} - H\hat{y} + \hat{\lambda}_x e - \hat{\lambda}_x H - \frac{e^2}{2} + eH \right) \tag{3.6}$$

3.2 Evaluation of the Navier-slip coefficient

To compare the two cases (smooth and micro-structured channel), the percent variation in volumetric flow rate $\Delta Q_{\%} = (\hat{u}_{bulk} - \hat{u}_0)/\hat{u}_0$ is defined, where $\hat{u}_0$ is the average velocity of the profile in the smooth channel and $\hat{u}_{bulk}$ is the average velocity of the flow in the lubricated one.
Starting with the expressions of the velocity profile of the fluid flow, the average velocity in both configurations are calculated:

$$\hat{u}_0 = -\frac{1}{\mu}\frac{\partial \hat{p}}{\partial \hat{x}}\frac{1}{3}H^2 \tag{3.7}$$

$$\hat{u}_{bulk} = \frac{1}{\mu}\frac{\partial \hat{p}}{\partial \hat{x}}\left[-\frac{H^2}{3} + eH - e^2 + \frac{e^3}{3H} + \hat{\lambda}_x\left(2e - \frac{e^2}{H} - H\right) - \frac{e^3}{12H}\right] \tag{3.8}$$

Consequently, $\Delta Q_{\%}$ assumes the following form:

$$\Delta Q_{\%} = \frac{\hat{u}_{bulk} - \hat{u}_0}{\hat{u}_0} = -\frac{3e}{H} + \frac{3e^2}{H^2} - \frac{e^3}{H^3} + \hat{\lambda}_x\left(\frac{3}{H} - \frac{6e}{H^2} + \frac{3e^2}{H^3}\right) \tag{3.9}$$

By rearranging equation 3.9, it's possible to extrapolate $\hat{\lambda}_x$ normalized by the parameter H, as a function of e and $\Delta Q_{\%}$:

$$\frac{\hat{\lambda}_x}{H} = \frac{\frac{3e}{H} - \frac{3e^2}{H^2} + \frac{e^3}{H^3} + \Delta Q_{\%}}{3 - \frac{6e}{H} + \frac{3e^2}{H^2}} \tag{3.10}$$

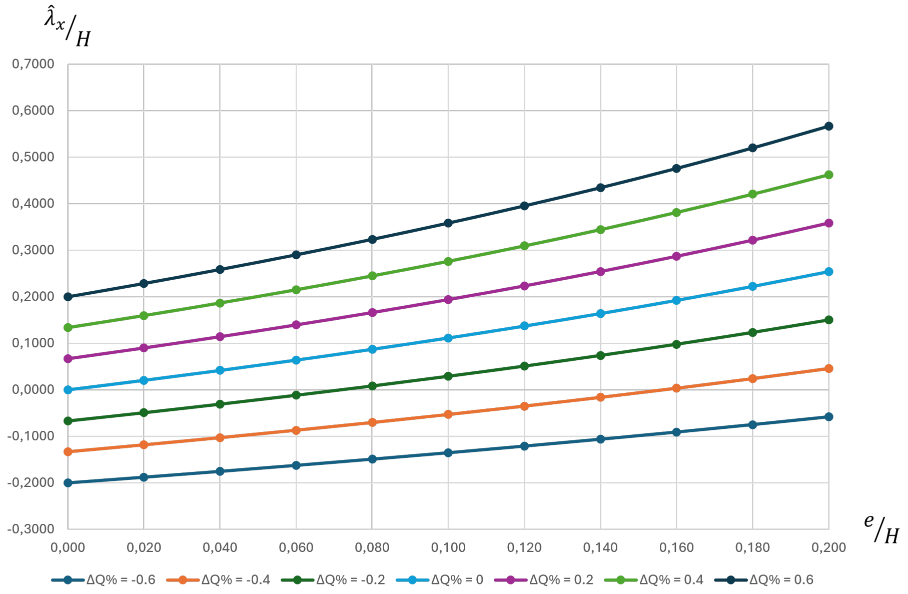

Figure 3.3: Trends for $\hat{\lambda}_x/H$ as a function of e/H at different values of $\Delta Q_{\%}$.

The values for $\hat{\lambda}_x/H$ are shown in figure 3.3, evaluated at different values of $\Delta Q_{\%}$. Basically, an increase in the size of the grooves, governed by the parameter e/H, involves a larger slip at the liquid-lubricant interface. This is consistent with the fact that there is a larger area of the solid surface where the wall shear stress is reduced. Furthermore, it is clear that an increase in the flow rate through the channel is reached when slip occurs, confirming the beneficial effects of the lubricant.

3.3 An additional scenario

A further case of fluid flow have been studied in the exact same way, just as a comparison. This time, only one side of the channel is infused with lubricant, whereas the other side is a simple solid wall.
The velocity profile for this case is:

$$\hat{u} = \frac{1}{\mu}\frac{\partial \hat{p}}{\partial \hat{x}}\left\{\frac{\hat{y}^2}{2} + \left(\frac{\hat{y}-2H}{e-2H}\right)\left[\hat{\lambda}_x\left(\frac{\frac{e^2}{2}-2eH+2H^2}{e-2H-\hat{\lambda}_x}\right)-\frac{e^2}{2}+2H^2\right]\right\}-2H^2 \tag{3.11}$$

Figure 3.4 shows the results found for this scenario.

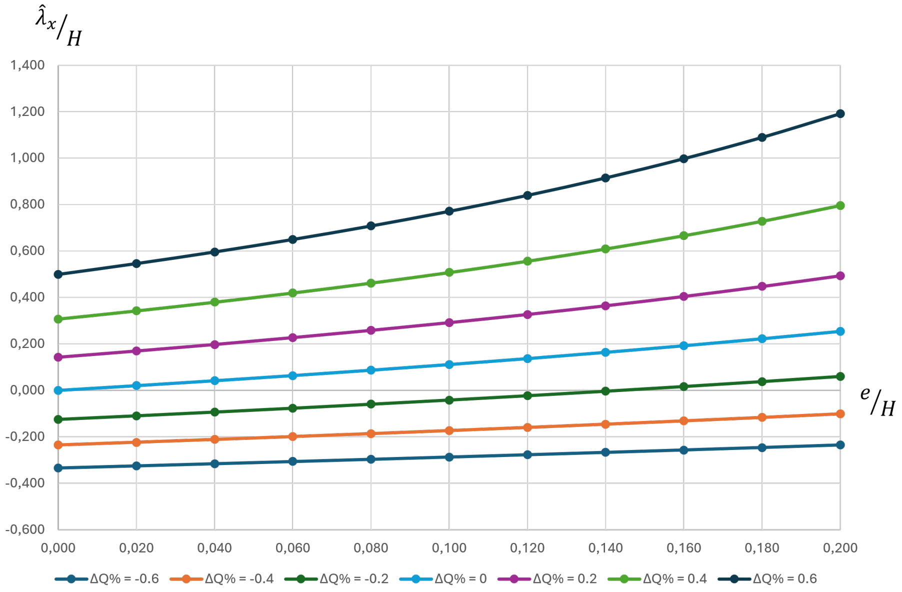

Figure 3.4: Trends for $\hat{\lambda}_x/H$ against e/H for different values of $\Delta Q_{\%}$.

The results confirm the expected behaviour of the non-symmetric channel, since for a specific geometry of the grooves, a larger slip $\hat{\lambda}_x$ is required to obtain the desired volumetric flow rate.

4 Asymptotic Homogenization

Solving a fluid flow over a rough wall is highly difficult. The flow is influenced by the micro-structured boundaries, where complex interactions take place as the fluid passes near the surface corrugations [11].
A common way to approach this type of problems is to apply the homogenization theory, which relies on the separation of scales, dividing the domain of interest into two different regions: the macroscopic region and the microscopic layer, each one characterised by a dimensional length scale.
By doing this, we can replace the solid wall with a virtual plane at which effective boundary conditions for the velocity are applied, to mimic the behaviour of the rough surface. Solving the fluid flow for the macroscopic region becomes much easier since we need no more to take into account details of near-wall fluid phenomena; the use of homogenization is thus particularly useful in numerical modelling of microtextured surfaces.
The aim is then to establish effective boundary conditions at the fictitious interface that match both the macroscopic and microscopic regions; the condition for homogenization to be applied is the separation of scale: we define the parameter ϵ, as the ratio of microscopic to macroscopic length scales

$$\epsilon = \frac{l}{L} << 1 \tag{4.1}$$

This parameter allows to tie the macroscopic and microscopic worlds.
The following dissertation about asymptotic homogenization is based on the analysis of a simple case of fluid flow over horizontal rough surface.

4.1 Governing equations and boundary conditions

The dimensional mass and momentum conservation equations governing the distribution of velocity are:

$$\frac{\partial \hat{u}_i}{\partial \hat{x}_i} = 0 \tag{4.2}$$

$$\rho\left(\frac{\partial \hat{u}_i}{\partial \hat{t}} + \hat{u}_j \frac{\partial \hat{u}_i}{\partial \hat{x}_j}\right) = -\frac{\partial \hat{p}}{\partial \hat{x}_i} + \mu \frac{\partial^2 \hat{u}_i}{\partial \hat{x}_j^2} \tag{4.3}$$

where $i = 1, 2, 3$ refers to the directions $\hat{x}, \hat{y}, \hat{z}$ and the velocity components are denoted as $\hat{u}_1 = \hat{u}$, $\hat{u}_2 = \hat{v}$, $\hat{u}_3 = \hat{w}$, ρ is the fluid density and μ is the dynamic viscosity of the bulk fluid.
We now define appropriate scales for the two regions. Note that from now on in this chapter we will refer to macroscopic parameters with capital case letters and to microscopic parameters with small case letters.

Macro-scales

- $L:$ length scale
- $\hat{U}:$ velocity scale
- $\rho\hat{U}^2:$ pressure scale
- $\dfrac{L}{\hat{U}}:$ time scale

Micro-scales

- $l:$ length scale
- $\hat{u}:$ velocity scale
- $\mu\dfrac{\hat{u}}{l}:$ pressure scale
- $\dfrac{l}{\hat{u}}:$ time scale

Once the scales are defined, we need to normalize every parameter of the governing equations to find the dimensionless equations of the problem.

Macro

- $X_i = \dfrac{\hat{X}_i}{L}$
- $U_i = \dfrac{\hat{U}_i}{\hat{U}}$
- $P = \dfrac{\hat{P}}{\rho\,\hat{U}^2}$
- $T = \dfrac{\hat{t}\,\hat{U}}{L}$

The dimensionless continuity equation is:

$$\frac{\partial U_i}{\partial X_i} = 0 \tag{4.4}$$

The dimensionless momentum equation is:

$$\frac{\partial U_i}{\partial T} + U_j\frac{\partial U_i}{\partial X_j} = -\frac{\partial P}{\partial X_i} + \frac{1}{Re}\frac{\partial^2 U_i}{\partial X_j^2} \tag{4.5}$$

where $Re = (\rho\hat{U}L)/\mu$ is the Reynolds number of the macroscopic problem.

Micro

- $x_i = \dfrac{\hat{x}_i}{l}$
- $u_i = \dfrac{\hat{u}_i}{\hat{u}}$
- $p = \dfrac{\hat{p}\, l}{\mu\, \hat{u}}$
- $t = \dfrac{\hat{t}\, \hat{u}}{l}$

The dimensionless continuity equation is:

$$\frac{\partial u_i}{\partial x_i} = 0 \tag{4.6}$$

The dimensionless momentum equation is:

$$\mathcal{R}\left(\frac{\partial u_i}{\partial t} + u_j \frac{\partial u_i}{\partial x_j}\right) = -\frac{\partial p}{\partial x_i} + \frac{\partial^2 u_i}{\partial x_j^2} \tag{4.7}$$

where $\mathcal{R} = (\rho l \hat{u})/\mu$ is the Reynolds number of the microscopic problem. Equation (4.7) can be rewritten as follows, since $\mathcal{R} = \epsilon^2 Re$:

$$\epsilon^2 Re\left(\frac{\partial u_i}{\partial t} + u_j \frac{\partial u_i}{\partial x_j}\right) = -\frac{\partial p}{\partial x_i} + \frac{\partial^2 u_i}{\partial x_j^2} \tag{4.8}$$

Boundary conditions of the problem

No-slip condition at the physical interface $\mathcal{I}_{\beta\sigma}$, between the fluid phase and the solid wall:

$$u_i = 0 \tag{4.9}$$

Continuity of the velocity vector at the virtual plane:

$$u_i|_{y=y_\infty} = \frac{1}{\epsilon} U_i\Big|_{Y=Y_\infty} \tag{4.10}$$

Continuity of the components of the traction vector at the interface between the two regions:

$$\left(\frac{\partial u_1}{\partial x_2} + \frac{\partial u_2}{\partial x_1}\right)\Big|_{y=y_\infty} = \left(\frac{\partial U_1}{\partial X_2} + \frac{\partial U_2}{\partial X_1}\right)\Big|_{Y=Y_\infty} \tag{4.11}$$

$$\left(-p+2\frac{\partial u_2}{\partial x_2}\right)\Bigg|_{y=y_\infty} = \left(-ReP+2\frac{\partial U_2}{\partial X_2}\right)\Bigg|_{Y=Y_\infty} \tag{4.12}$$

$$\left(\frac{\partial u_3}{\partial x_2}+\frac{\partial u_2}{\partial x_3}\right)\Bigg|_{y=y_\infty} = \left(\frac{\partial U_3}{\partial X_2}+\frac{\partial U_2}{\partial X_3}\right)\Bigg|_{Y=Y_\infty} \tag{4.13}$$

4.2 Asymptotic analysis

An asymptotic analysis is then conducted on the microscopic problem, which is reconstructed at different orders of the parameter ϵ. Every variable of the problem is expressed in the following form:

$$f = \epsilon^0 f^{(0)} + \epsilon^1 f^{(1)} + \epsilon^2 f^{(2)} + \dots + \epsilon^n f^{(n)} \tag{4.14}$$

So, for example, the velocity components and the pressure are:

$$u_i = \epsilon^0 u_i^{(0)} + \epsilon^1 u_i^{(1)} + \epsilon^2 u_i^{(2)} + \dots + \epsilon^n u_i^{(n)} \tag{4.15}$$

$$p = \epsilon^0 p^{(0)} + \epsilon^1 p^{(1)} + \epsilon^2 p^{(2)} + \dots + \epsilon^n p^{(n)} \tag{4.16}$$

Assuming that the macroscopic and microscopic variables are independent, the chain rule for the derivation becomes:

$$\frac{\partial}{\partial x_i} \rightarrow \frac{\partial}{\partial x_i} + \epsilon\frac{\partial}{\partial X_i} \tag{4.17}$$

$$\frac{\partial^2}{\partial x_i^2} \rightarrow \frac{\partial^2}{\partial x_i^2} + \epsilon^2\frac{\partial^2}{\partial X_i^2} + 2\epsilon\frac{\partial^2}{\partial x_i \partial X_i} \tag{4.18}$$

Let's now introduce the asymptotic progressions in the homogenized microscopic equations, reconstructed at the primary order $O(\epsilon^0)$.
Continuity equation:

$$\frac{\partial u_i^{(0)}}{\partial x_i} = 0 \tag{4.19}$$

Momentum equation:

$$-\frac{\partial p^{(0)}}{\partial x_i} + \frac{\partial^2 u_i^{(0)}}{\partial x_j^2} = 0 \tag{4.20}$$

Boundary conditions:

$$u_i^{(0)} = 0 \qquad at \;\; \mathcal{I}_{\beta\sigma} \tag{4.21}$$

$$\left(\frac{\partial u_1^{(0)}}{\partial x_2} + \frac{\partial u_2^{(0)}}{\partial x_1}\right)\Bigg|_{y=y_\infty} = \; S_{12} \tag{4.22}$$

$$\left(-p^{(0)} + 2\frac{\partial u_2^{(0)}}{\partial x_2}\right)\Bigg|_{y=y_\infty} = \; S_{22} \tag{4.23}$$

$$\left(\frac{\partial u_3^{(0)}}{\partial x_2} + \frac{\partial u_2^{(0)}}{\partial x_3}\right)\Bigg|_{y=y_\infty} = \; S_{32} \tag{4.24}$$

where S_{12}, S_{22}, S_{32} are the components of the traction vector $\mathbf{S}$, exerted on the surface at y_∞ by the external (macroscopic) fluid flow.

Since the problem, given by equations from 4.19 to 4.24, is linear and forced by the traction vector $\mathbf{S}$, a generic solution of the problem can be expressed in the following form:

$$\begin{cases} u_1^{(0)} = u_{11}^{\dagger} S_{12} + u_{12}^{\dagger} S_{22} + u_{13}^{\dagger} S_{23} \\ u_2^{(0)} = u_{21}^{\dagger} S_{12} + u_{22}^{\dagger} S_{22} + u_{23}^{\dagger} S_{23} \\ u_3^{(0)} = u_{31}^{\dagger} S_{12} + u_{32}^{\dagger} S_{22} + u_{33}^{\dagger} S_{23} \\ p^{(0)} = p_1^{\dagger} S_{12} + p_2^{\dagger} S_{22} + p_3^{\dagger} S_{23} \end{cases} \tag{4.25}$$

The parameters marked with the "†" sign are called auxiliary variables.

In order to solve the problem, it is necessary to substitute every variable $u_i^{(0)}$ and $p^{(0)}$ in the dimensionless Navier-Stokes equations and boundary conditions, which will give the values for the auxiliary variables.

4.3 Effective boundary conditions

For an incompressible, steady, laminar flow in a channel bounded by a rough wall, dimensional effective boundary conditions valid up to second-order $O(\epsilon^2)$ are:

$$\hat{u}|_{\hat{y}=0} = \hat{\lambda}_x \left(\frac{\partial \hat{u}}{\partial \hat{y}} + \frac{\partial \hat{v}}{\partial \hat{x}}\right)\Bigg|_{\hat{y}=0} + \frac{\hat{k}_{xy}^{itf}}{\mu}\frac{\partial}{\partial \hat{x}}\left(-\hat{p} + 2\mu\frac{\partial \hat{v}}{\partial \hat{y}}\right)\Bigg|_{\hat{y}=0} \tag{4.26}$$

$$\hat{v}|_{\hat{y}=0} = -k_{xy}^{itf}\frac{\partial}{\partial \hat{x}}\left(\frac{\partial \hat{u}}{\partial \hat{y}} + \frac{\partial \hat{v}}{\partial \hat{x}}\right)\Bigg|_{\hat{y}=0} - k_{zy}^{itf}\frac{\partial}{\partial \hat{z}}\left(-\hat{p} + 2\mu\frac{\partial \hat{v}}{\partial \hat{y}}\right)\Bigg|_{\hat{y}=0} \tag{4.27}$$

$$\hat{w}|_{\hat{y}=0} = \hat{\lambda}_z \left(\frac{\partial \hat{w}}{\partial \hat{y}} + \frac{\partial \hat{v}}{\partial \hat{z}}\right)\Bigg|_{\hat{y}=0} + \frac{\hat{k}_{zy}^{itf}}{\mu}\frac{\partial}{\partial \hat{z}}\left(-\hat{p} + 2\mu\frac{\partial \hat{v}}{\partial \hat{y}}\right)\Bigg|_{\hat{y}=0} \tag{4.28}$$

evaluated at $\hat{y} = 0$.

The new parameters of the boundary conditions, $\hat{\lambda}_x$, $\hat{\lambda}_z$, $\hat{k}^{itf}_{xy}$, $\hat{k}^{itf}_{zy}$, correspond to the auxiliary variables that come from asymptotic analysis.

In particular, $\hat{\lambda}_x$ and $\hat{\lambda}_z$ are the components of the Navier-slip vector $\hat{\lambda} = (\hat{\lambda}_x, 0, \hat{\lambda}_z)$, also called effective slip length, while $\hat{k}^{itf}_{xy}$ and $\hat{k}^{itf}_{zy}$ are the components of a second order tensor and are called interface permeability coefficients.

The auxiliary variables $(\hat{\lambda}_x, \hat{\lambda}_z, \hat{k}^{itf}_{xy}, \hat{k}^{itf}_{zy})$ are homogeneous to, respectively, a length and a surface area, and correspond to the product of their dimensionless counterpart times l and l^2:

$$\hat{\lambda}_x = \lambda_x \, l \tag{4.29}$$

$$\hat{\lambda}_z = \lambda_z \, l \tag{4.30}$$

$$\hat{k}^{itf}_{xy} = k^{itf}_{xy} \, l^2 \tag{4.31}$$

$$\hat{k}^{itf}_{zy} = k^{itf}_{zy} \, l^2 \tag{4.32}$$

These coefficients are intrinsic to the geometric characteristics of the boundary, and do not depend on the Reynolds number.

5 Modelling and Simulation of Superhydrophobic and Liquid-Infused Surfaces

Numerical simulations of laminar flow were performed to evaluate the slip parameters λ_x and λ_z over superhydrophobic and liquid-infused surfaces, using water as working fluid. To have a better understanding of these classes of surfaces we studied both the streamwise and spanwise configurations, analyzing the behaviour for different values of depletion and the characteristic groove's size α (ranging from 0.1 to 0.8).
The data collected from simulations have been processed to get the results shown in the following.

5.1 CFD software

STAR-CCM+ by CD-Adapco is the main software we used for simulations, though we adopted also COMSOL Multiphysics for several cases.
STAR-CCM+ is a computational fluid dynamics software that enables to simulate multi-physics systems that operate in real conditions, in both 2D and 3D.
To run a simulation on this software, the following steps need to be done:

- Definition of all the parameters and field functions;
- Design of the geometry of the problem;
- Set up of the boundary conditions for the domain;
- Mesh generation;
- Visualization and analysis of the results.

A brief sketch of the domain we studied is reported in figure 5.1, where l is the pitch distance of the unit cell, α is the lubricant surface area, d is the depletion of lubricant and y_∞ is the height of the unit cell.
To evaluate the effective slip length, the software solves a Laplace problem for the velocity field. A flux in the direction perpendicular to that of the domain is imposed on the upper boundary to establish the desired fluid flow.
The mesh can be built in polygonal, triangular or rectangular cells; the finer the mesh the more accurate the results will be. A very useful feature for our work, was the possibility to make a finer mesh in the lower part of the domain, where slip occurs, and leaving a coarser mesh in rest of it to ease the overall calculations.

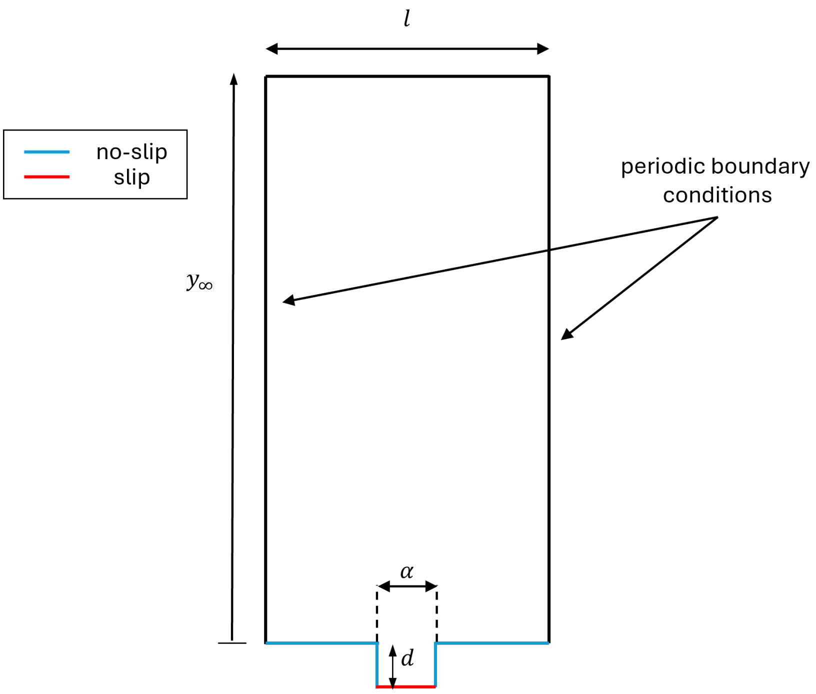

Figure 5.1: Sketch of the domain used for simulations. The desired boundary conditions are imposed on every side: zero-shear stress (red line), no-slip (blue line), periodic flow conditions (lateral sides) and imposed flux (upper side).

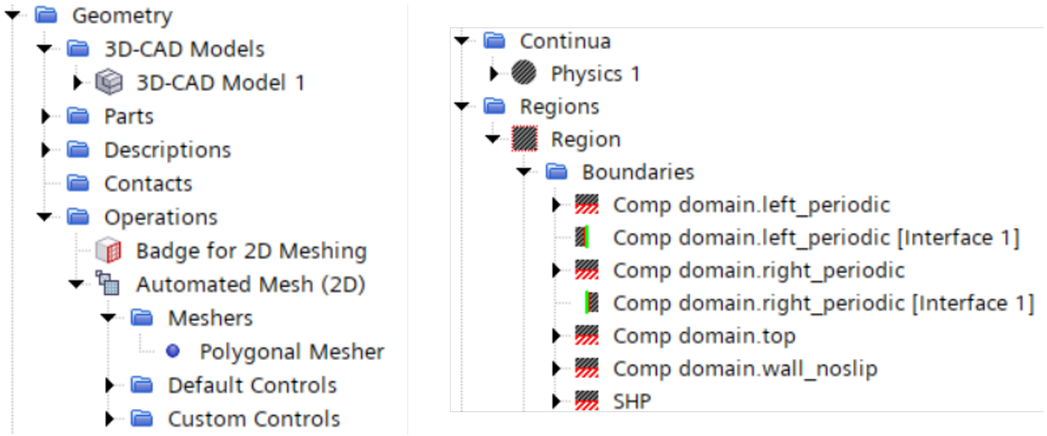

Figure 5.2: Settings for the geometry and boundary conditions in a Star-CCM+ simulation.

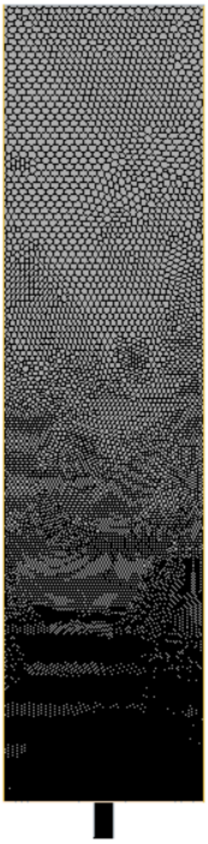

Figure 5.3: Mesh of the entire domain.

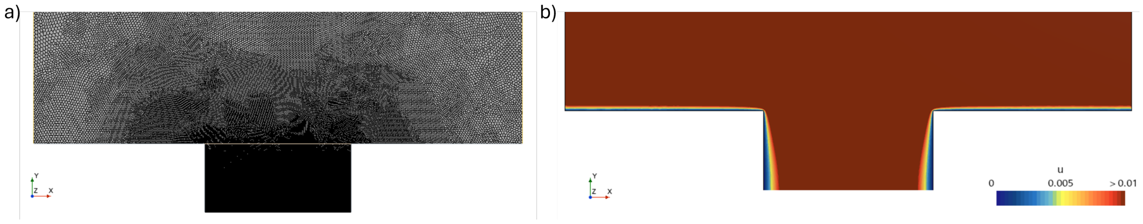

Figure 5.4: (a) Lower part of the domain with a finer mesh. (b) Velocity field during a simulation.

5.2 Superhydrophobic surfaces

It is well known from literature, that the amount of slip, quantified by the slip length, is mainly associated to the structural features of the surface and affected by the state of the liquid gas interface [12].
Direct numerical simulations over longitudinal superhydrophobic square grooves show that the ratio λ_x/λ_z, for the values we found, is constant and equal to 2 for no depletion, as shown by figure 5.5 (black solid line in the figure). This is in agreement with the relation by Philip (1972) [13]:

$$\lambda_x = 2\lambda_z = \frac{l}{\pi} ln\left\{sec\left[\frac{\pi}{2}(1-\phi_s)\right]\right\} \tag{5.1}$$

where l is the pitch distance of the domain and ϕ_s is the solid area fraction, which corresponds to α_{sh} in our study.
As depletion increases, the maximum value of the ratio λ_x/λ_z is shifted to larger values of α_{sh}.

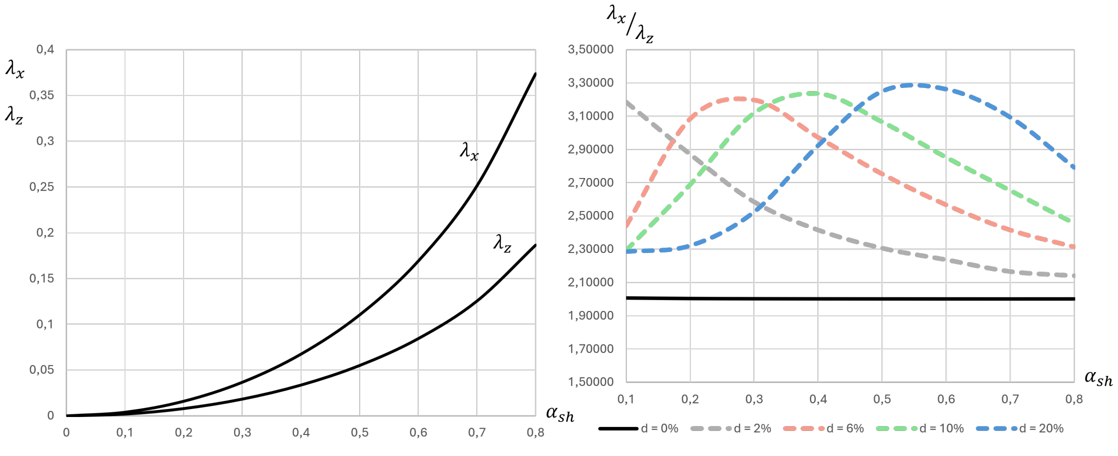

Figure 5.5: λ_x and λ_z against α_{sh} for no depletion (left). Trends for the ratio λ_x/λ_z against α_{sh} for different values of depletion (right).

The first results are then in good agreement with previous studies.
By studying the behavior of slip, we noticed that the main parameters affecting the slip coefficients are the depletion d and the groove's size α_{sh}.
The following figures are the processed results from simulations. In general, the depletion affects negatively the slip at the liquid-gas interface [8]. Instead, as the groove's size increases, the slip increases too, as expected by the theoretical formulation in chapter 3.

Streamwise configuration

This section presents the results for longitudinal square grooves.
Three pairs of figures show the Navier slip coefficients λ_x and λ_z as functions of the depletion and the groove's size.

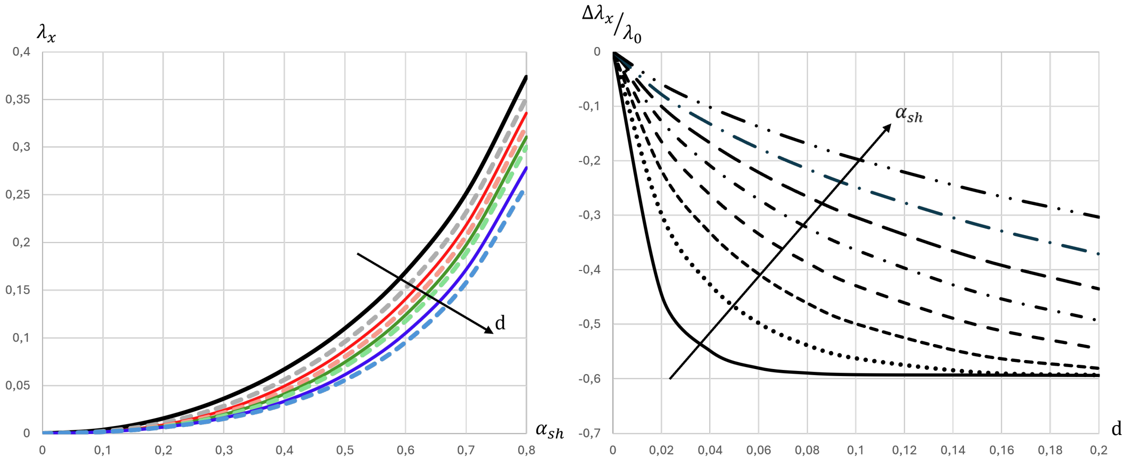

Figure 5.6: Trends for λ_x as a functions of α_{sh} for different values of depletion (left). Trends for the deviation of λ_x in respect of λ_x in the case of zero depletion, as a function of d, for different values of α_{sh} (right).

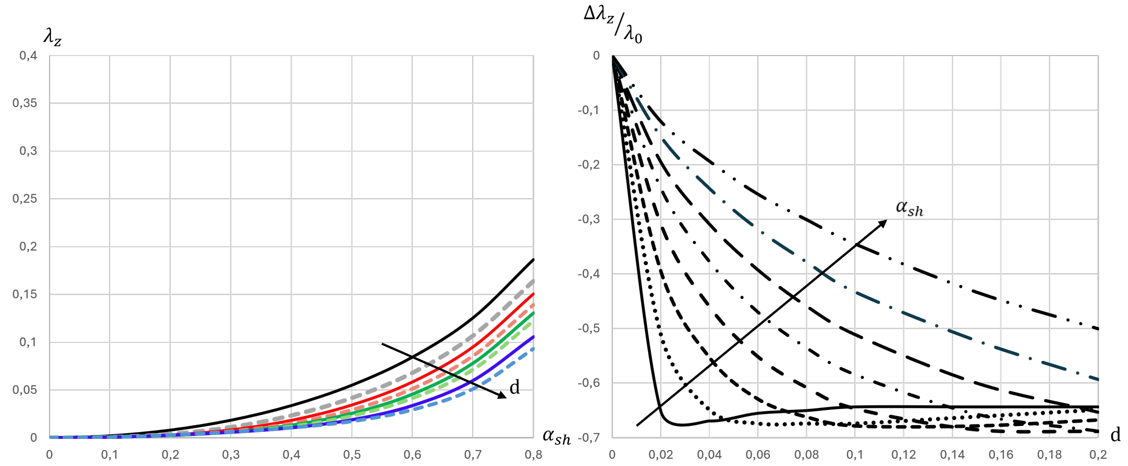

Figure 5.7: Trends for λ_z as a functions of α_{sh} for different values of depletion (left). Trends for the deviation of λ_z in respect of λ_z in the case of zero depletion, as a function of d, for different values of α_{sh} (right).

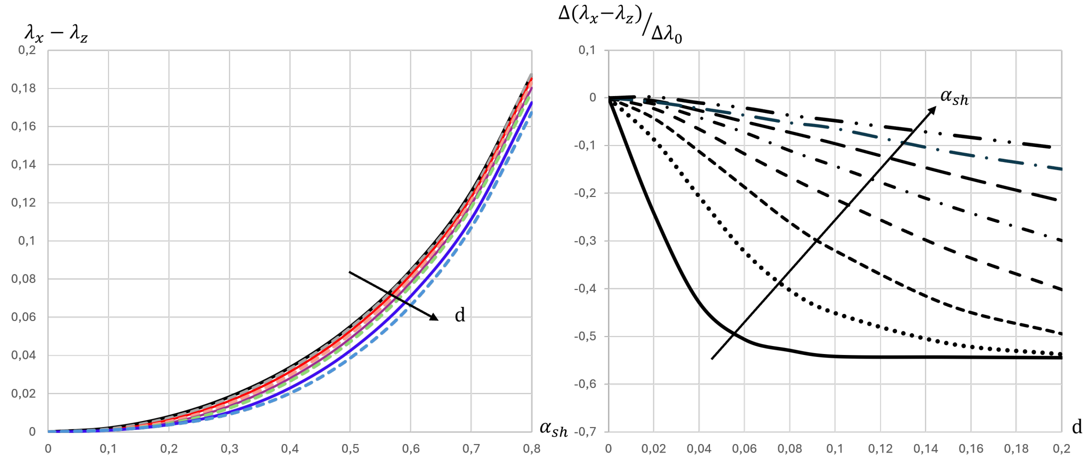

Figure 5.8: Trends for $\lambda_x - \lambda_z$ as a functions of α_{sh} for different values of depletion (left). Trends for the deviation of $\lambda_x - \lambda_z$ in respect of $\lambda_x - \lambda_z$ in the case of zero depletion, as a function of d, for different values of α_{sh} (right).

Considering the left images, λ_x is much larger than λ_z for the longitudinal case. Also, an increase in the depletion always worsen the slippage, as expected. The values of d go from 0% to 20%.
Right figures plot $(\lambda - \lambda_0)/\lambda_0$, which is the deviation of λ in respect of the value of λ in case of no depletion, against d.

Spanwise configuration

The same study has been conducted in case of transverse square grooves.
The results for this configuration, conversely to the longitudinal case, show that λ_z is much larger than λ_x. But, aside from that, the surface reacts in the same way when it comes to change the values of depletion and groove's size.

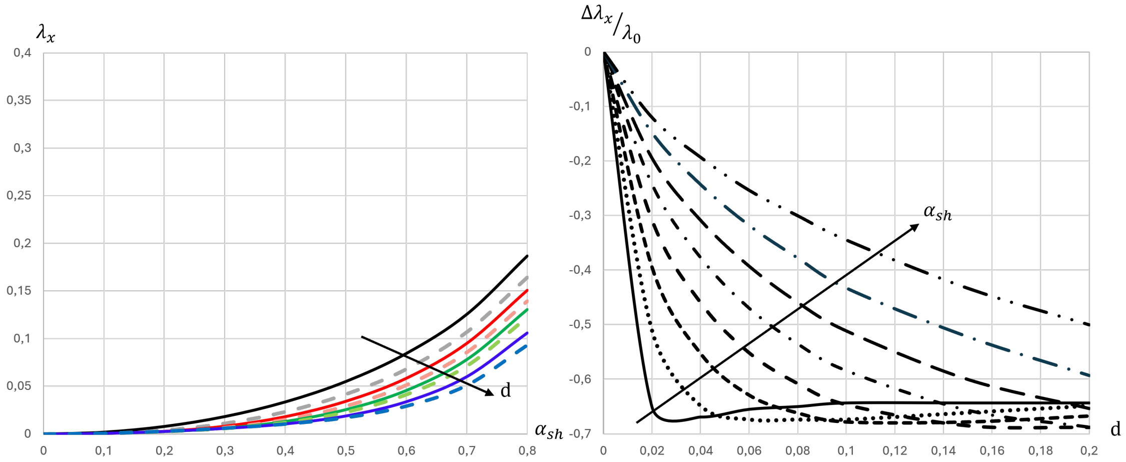

Figure 5.9: Trends for λ_x as a functions of α_{sh} for different values of depletion (left). Trends for the deviation of λ_x in respect of λ_x in the case of zero depletion, as a function of d, for different values of α_{sh} (right).

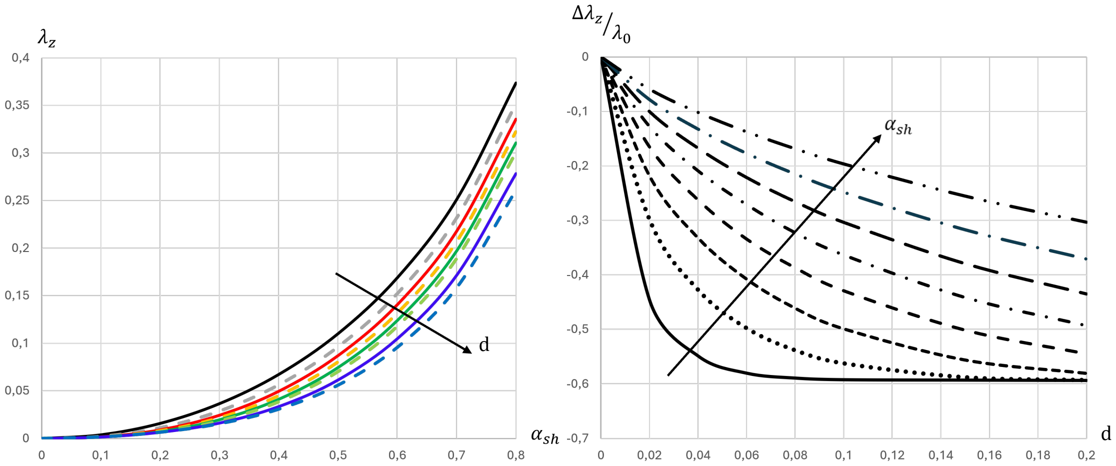

Figure 5.10: Trends for λ_z as a functions of α_{sh} for different values of depletion (left). Trends for the deviation of λ_z in respect of λ_z in the case of zero depletion, as a function of d, for different values of α_{sh} (right).

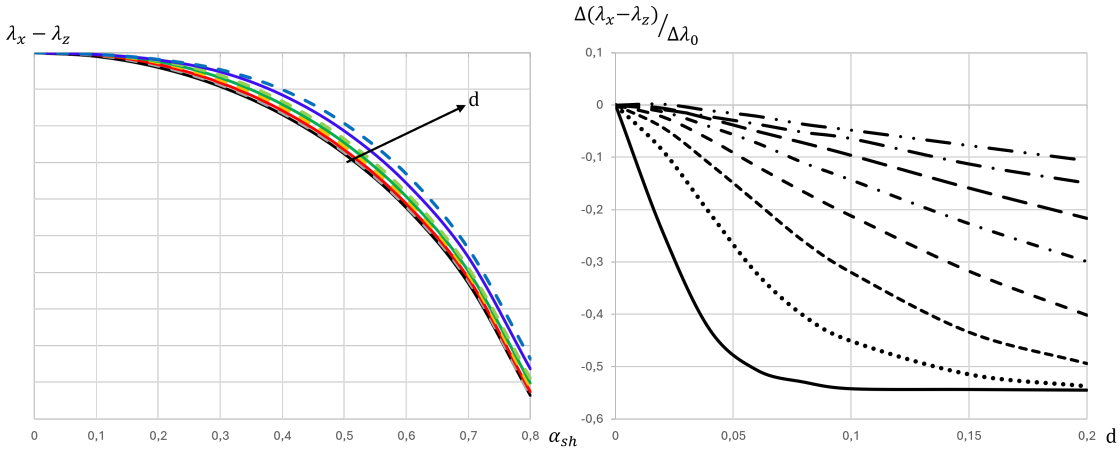

Figure 5.11: Trends for $\lambda_x - \lambda_z$ as a functions of α_{sh} for different values of depletion (left). Trends for the deviation of $\lambda_x - \lambda_z$ in respect of $\lambda_x - \lambda_z$ in the case of zero depletion, as a function of d, for different values of α_{sh} (right).

5.3 MATLAB code

By combining the theoretical approach and the results from numerical simulations, a simple MATLAB code has been developed to create something useful and concrete for users.

Symmetric and non-symmetric channels from chapter 3 are the scenarios where this code is applied. All the values of the slip coefficients λ_x and λ_z, from simulations, are stored in form of matrixes. Once the code is run, it is asked to the user to set the parameters of the problem: the orientation of external flow in respect of the grooves, the ratio e/H, the ratio l/H and the desired value of α.

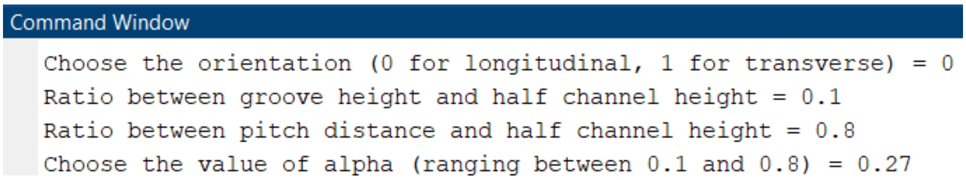

```
Choose the orientation (0 for longitudinal, 1 for transverse) = 0
Ratio between groove height and half channel height = 0.1
Ratio between pitch distance and half channel height = 0.8
Choose the value of alpha (ranging between 0.1 and 0.8) = 0.27
```

Figure 5.12: Settings of the desired parameters for the case of analysis.

Figure 5.12 shows an example of application where $\alpha = 0.27$. The code works also for values of α that are not strictly the ones we used in simulations, but are in between of them. This is possible thanks to a linear extrapolation.

The output is composed of two graphs: the upper one shows the trends for λ_x, λ_z and $\lambda_x - \lambda_z$ against the percentage of depletion. In the lower one there are the trends for volumetric flow rate $\Delta Q_{\%}$ and the pressure gradient $\Delta forcing_{\%}$, both in respect of the baseline case of figure 3.1.

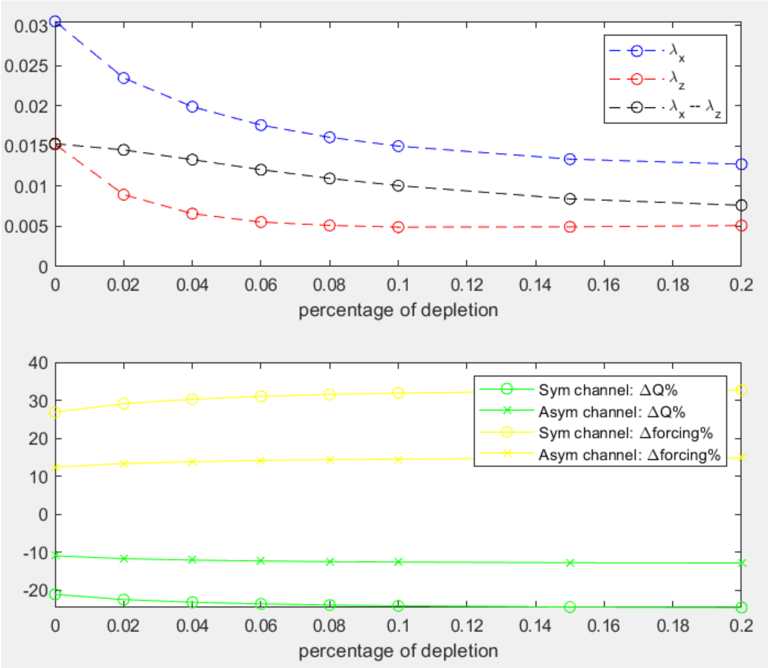

Figure 5.13: Output of the code.

5.4 Liquid-infused surfaces

5.4.1 Numerical approach

Numerical simulations have been performed over LIS. We investigated the behaviour of three different liquid lubricants and compared the results with the superhydrophobic case. The lubricants at issue are: heptane ($\mu_R = 0.37$), FC-3283 ($\mu_R = 1.5$) and FC-70 ($\mu_R = 23$). The viscosity ratio μ_R is defined as the ratio between the viscosity of the lubricant and the one of water.
This time, the simulations require to study a multi-phase fluid flow in the domain. The slip coefficients are evaluated at the fluid-fluid interface, considering also few cases of depletion for the lubricant.
The results obtained are shown in figure 5.14, and they are quite surprising. It is clear from the figure that depletion plays a very important role. However, something unexpected related to the viscosity ratio happens. It seems that this parameter mainly influences the slipping effect, and worsen the performance of the surface when $\mu_R > 1$.

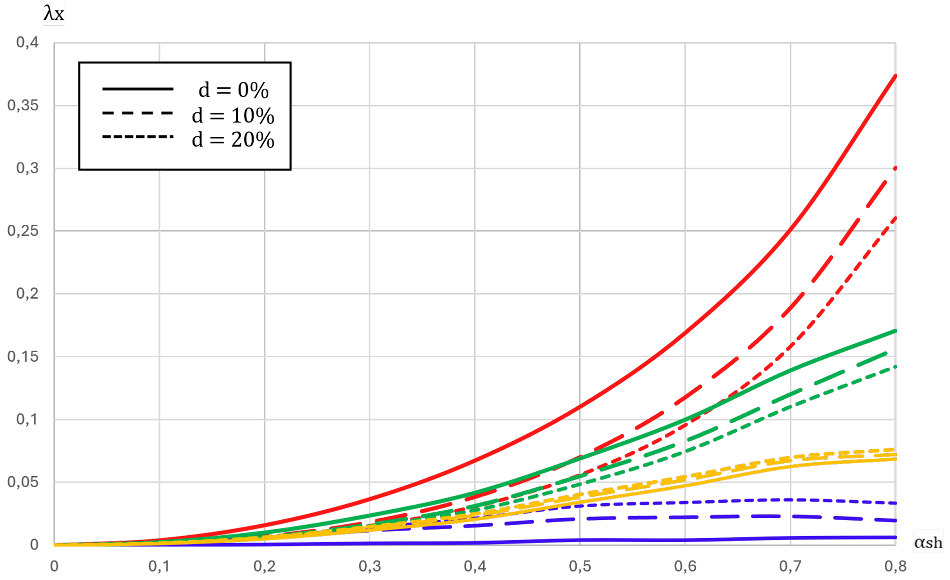

Figure 5.14: Trends for the coefficient λ_x against α for different types of lubricant: air $\mu_R = 0.018$ (red lines), heptane $\mu_R = 0.37$ (green lines), FC-3283 $\mu_R = 1.5$ (yellow lines) and FC-70 $\mu_R = 23$ (blue lines).

Indeed, when $\mu_R < 1$, the liquid lubricant provides a good effect in terms of slip length, showing a behaviour similar to the case of air. Nevertheless, as μ_R becomes slightly larger than 1, such as for the FC-3283, the slippage of the surfaces almost vanish to the point of a no-slip condition, jeopardising every benefits from infusing the solid surface with a lubricant.
Another interesting point is that, when $\mu_R > 1$ the depletion seems to have a positive effect. This could be explained with the fact that the larger the depletion, the less lubricant with a high viscosity is present on the surface.

5.4.2 A look into the literature

A comparison between two studies from the literature have been conducted to have a wider overview on the effect of viscosity ratio on LIS.
First, we evaluated the slip coefficients λ_x and λ_z using a theoretical relation from Belyaev & Vinogradova (2010) [14]. They studied superhydrophobic surfaces with alternating slip and no-slip areas, and proposed an analytical relation between the effective slip lengths and surface geometric parameters for longitudinal ($x_i = x$) and transverse ($x_i = z$) groove configurations [15]:

$$\lambda_{x_i} \simeq \frac{l \ln\left[\sec\left(\frac{\pi\alpha}{2}\right)\right]}{K_i + \frac{l}{\bar{\lambda}_{x_i}} \ln\left[\sec\left(\frac{\pi\alpha}{2}\right) + \tan\left(\frac{\pi\alpha}{2}\right)\right]} \tag{5.2}$$

where l is the pitch distance in laminar case, $K_i = \pi$ and 2π for the longitudinal and transverse grooves, respectively, and $\bar{\lambda}_{x_i}$ are the constant slip lengths defined as:

$$\bar{\lambda}_x = \frac{1.12}{\pi} \mu_R e \tanh\left(\frac{\pi D}{e}\right) \tag{5.3}$$

$$\bar{\lambda}_z = \frac{0.342}{\pi} \mu_R e \tanh\left(\frac{\pi D}{e}\right) \tag{5.4}$$

Then, we extrapolated the values of λ_x and λ_z from a numerical study by Bottaro *et al.* (2018) [16], and compared the results.

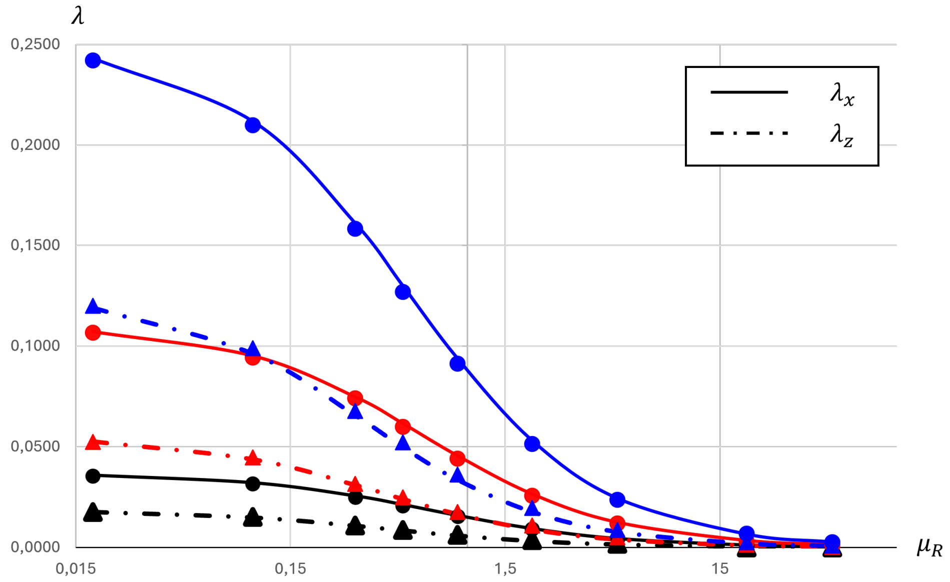

Figure 5.15: Trends for the effective slip length against μ_R, ranging from 0.018 to 50, at $\alpha = 0.3$ (black), $\alpha = 0.5$ (red) and $\alpha = 0.7$ (blue). The lines represent the values of λ evaluated from the theoretical relation, whereas the symbols (circles for longitudinal and triangles for transverse) are the values of the slip length from Bottaro et al. (2018) [16].

Figure 5.15 shows the trends for the effective slip length λ, in both longitudinal (λ_x) and transverse (λ_z) configurations, as function of the viscosity ratio μ_R, for three different values of the parameter α.
The results from the theoretical relation match very well those from the numerical study [16]. Moreover, the trends from these results confirm what we previously have found about the great influence of viscosity ratio. As μ_R increases, the slipping effect is reduced, up to vanishing at some point. Plus, the geometric features of the surface significantly influences this large drop in λ due to the viscosity ratio, as shown by the blue lines in the figure, that represent the case $\alpha = 0.7$.
What emerges from this study is that infusing a surface with a liquid lubricant not necessary brings to a drag reduction. If the viscosity of the lubricant is much larger than that of the external fluid, it could even worsen the surface to the point of a drag increase.

6 What about Turbulence?

A brief investigation of a turbulent fluid flow over lubricant-infused surfaces (SHS and LIS) has been conducted to understand the effect of slip on turbulence.
First of all, to set up the turbulent problem, it is necessary to define the pitch distance in wall units:

$$l^+ = \frac{\rho u_\tau l}{\mu} \tag{6.1}$$

The parameter $u_\tau = \sqrt{\tau_w/\rho}$, defined in the conventional manner with respect to the wall shear stress, is the friction velocity, and τ_w is the shear stress exerted by the external fluid on the surface. Similarly, the Navier-slip coefficients can be expressed in wall units as

$$\lambda_x^+ = \frac{\rho u_\tau \hat{\lambda}_x}{\mu} = l^+ \lambda_x \tag{6.2}$$

$$\lambda_z^+ = \frac{\rho u_\tau \hat{\lambda}_z}{\mu} = l^+ \lambda_z \tag{6.3}$$

To evaluate λ_x and λ_z, we used the theoretical relation 5.2, discussed in the previous chapter.

For small values of l^+, we can assume the difference between λ_x^+ and λ_z^+ to be equal to the roughness function ΔU^+:

$$\Delta\lambda^+ = \lambda_x^+ - \lambda_z^+ = \Delta U^+ \tag{6.4}$$

The friction factor, expressed as a power series of the parameter A up to third order, is defined in respect of a smooth channel case:

$$\frac{\Delta c_f}{c_{f_0}} = \frac{c_{f_i} - c_{f_0}}{c_{f_0}} = \frac{A^3}{8} - \frac{A^2}{2} + A \tag{6.5}$$

The parameter A is expressed by the following relation:

$$A = \frac{\Delta U^+}{(2c_{f_0})^{-\frac{1}{2}} + (2k)^{-1}} \tag{6.6}$$

where $k = 0.4$ is the von Kármán constant and $c_{f_0} \approx 0.00813$ for the case of smooth channel when $Re_\tau = 180$. Simply, the drag reduction (DR) is equal to $-\dfrac{\Delta c_f}{c_{f_0}}$.

The results we propose in the following tables are compared to those reached by Chang *et. al* (2019) [15].
The three lubricants for this study are air (SHS), heptane (LIS) and FC-70 (LIS). The parameter α is set to 0.8, while the ratio between the depth of the groove and the pitch distance l changes for every case in the way shown by table 6.1.

	Viscosity ratio μ_R	Depth / l	λ_x	λ_z
1	0.018	0.08 / 0.021	0.361	0.176
2	0.37	0.04 / 0.021	0.212	0.083
3	23	0.02 / 0.021	0.008	0.002
4	0.018	0.08 / 0.042	0.361	0.176
5	0.37	0.04 / 0.042	0.212	0.083
6	23	0.02 / 0.042	0.007	0.002
7	0.018	0.08 / 0.084	0.361	0.176
8	0.37	0.04 / 0.084	0.208	0.081
9	23	0.02 / 0.084	0.006	0.002

Table 6.1: Effective slip length values for different lubricant and geometric features

The values of λ_x and λ_z, evaluated with equation 5.2, are then multiplied by three different values of l^+, to eventually find the percentage drag reduction up to third order, with equation 6.5. The last column of table 6.2 shows the percentage drag reduction from the mentioned study.

	Viscosity ratio μ_R	l^+	DR %	DR % [15]
1	0.018	3.78	5.89 %	7 %
2	0.37	3.78	4.16 %	4.6 %
3	23	3.78	0.18 %	/
4	0.018	7.56	11.42 %	12.7 %
5	0.37	7.56	8.14 %	9.1 %
6	23	7.56	0.34 %	/
7	0.018	15.12	21.5 %	21.1 %
8	0.37	15.12	15.37 %	12.7 %
9	23	15.12	0.52 %	/

Table 6.2: Drag reduction results and comparison with a study from the literature.

The values of drag reduction that we found are in well agreement with the work by Chang *et al.* (2019) [15].
Also in turbulent flows, air maintains the best performance, while increasing the viscosity of the lubricant brings in the inevitable decrease of drag reduction. In addition, another time, a larger geometry feature improves the ability of the surface in reducing friction drag, but the case $\mu_R >> 1$ is always almost useless.
Due to the complexity of the turbulent problem, further studies are necessary to fully explore the effect of lubricant-infused surfaces under different circumstances.

7 Conclusions

In this study, we investigated the slip occurring at fluid-fluid interface when a solid surface is infused with lubricant. The work provides numerical evidences of the drag reduction that can be achieved by lubricant-infused surfaces, in both laminar and turbulent fluid flows, and also an overview on asymptotic homogenization. The performance of superhydrophobic and liquid-infused surfaces have been analyzed and compared.

The results obtained, based on effective boundary conditions of the slip velocities, confirm the well known dominance of SHS in reducing drag, but also demonstrate that LIS can achieve values of drag reduction comparable to those reached by SHS, until $\mu_R < 1$. This is particularly significant for future applications, thanks to the interface stability that a liquid lubricant can guarantee. In addition, to have a wider understanding of the problem, each case have been tested for different values of depletion and α.

A simple MATLAB code was created to allows users to quantify the slip length and the percentage change in the flow rate for the laminar flow in a channel bounded be infused walls, requiring only to set the geometric features of the problem. Further, some theoretical calculations of the drag reduction caused by SHS and LIS under turbulence were done and the results were found to be in good agreement with findings from the literature, confirming the validity of the work.

Along with the fascination of the physical and mathematical study of fluid flows over slippery surfaces, the aim of this research is to help the design of such surfaces in order to implement them in practical engineered applications.

References

[1] M. K. Fu, I. Arenas, S. Leonardi, and M. Hultmark. Liquid-infused surfaces as a passive method of turbulent drag reduction. *Journal of Fluid Mechanics*, 824:688–700, 2017.

[2] A. K. Epstein, T.-S.Wong, R. A. Belisleand E. M. Boggs, and J. Aizenberg. Liquid-infused structured surfaces with exceptional anti-biofouling performance. *PNAS*, 109:13182–13187, 2012.

[3] T. V. Charpentier, A. Neville, S. Baudin, M. J. Smith, M. Euvrard, A. Bell, C. Wang, and R. Barker. Liquid infused porous surfaces for mineral fouling mitigation. *Journal of colloid and interface science*, 444, 2015.

[4] B. R. Solomon, K. S. Khalil, and K. K. Varanasi. Drag reduction using lubricant-impregnated surfaces in viscous laminar flow. *Langmuir*, 30:10970, 2014.

[5] S. J. Lee, H. N. Kim, W. Choi, G. Y. Yoon, and E. Seo. A nature-inspired lubricant-infused surface for sustainable drag reduction. *Soft Matter*, 15:8459, 2019.

[6] J. Sundin, U. Ciri, S. Leonardi, M. Hultmark, and S. Bagheri. Heat transfer increase by convection in liquid-infused surfaces for laminar and turbulent flows. *Journal of Fluid Mechanics*, 941, 2022.

[7] T. Van Buren and A. J. Smits. Substantial drag reduction in turbulent flow using liquid-infused surfaces. *Journal of Fluid Mechanics*, 827:448–456, 2017.

[8] C. Vega-Sánchez and C. Neto. Slightly depleted lubricant-infused surfaces are no longer slippery. *Langmuir*, 38:10568–10574, 2022.

[9] C. Vega-Sánchez, S. Peppou-Chapman, L. Zhu, and C. Neto. Nanobubbles explain the large slip observed on lubricant-infused surfaces. *Nat Commun*, 13:351, 2022.

[10] S. Peppou-Chapman, C. Vega-Sánchez, and C. Neto. Detection of nanobubbles on lubricant-infused surfaces using afm meniscus force measurements. *Langmuir*, 38:10234–10243, 2022.

[11] E. N. Ahmed and A. Bottaro. Laminar flow in a channel bounded by porous/rough walls: Revisiting beavers-joseph-saffman. *European Journal of Mechanics/B Fluids*, 103:269–283, 2024.

[12] A. Bottaro. Homogenized boundary conditions for micro-textured surfaces. *50+ Years of AIMETA*, pages 383–397, 2022.

[13] J. R. Philip. Flows satisfying mixed no-slip and no-shear conditions. *ZAMP*, 23:353–372, 1972.

[14] A. V. Belyaev and O. I. Vinogradova. Effective slip in pressure-driven flow past superhydrophobic stripes. *Journal of Fluid Mech.*, 652:489–499, 2010.

[15] J. Chang, T. Jung, H. Choi, and J. Kim. Predictions of the effective slip lenght and

drag reduction with a lubricated micro-groove surface in a turbulent channel flow. *Journal of Fluid Mechanics*, 874:797–820, 2019.

[16] E. Alinovi and A. Bottaro. Apparent slip and drag reduction for the flow over superhydrophobic and lubricant-impregnated surfaces. *Physical Review Fluids*, 3(12):124002, 2018.